

Optimized online filter stack spectrometer for ultrashort X-ray pulses*

Jia-Xing Wen^{1,2}, Ge Ma^{3,2}, Ming-Hai Yu¹, Yu-Chi Wu¹, Yong-Hong Yan¹, Shao-Yi Wang¹, Huai-Zhong Gao^{3,2}, Lu-Shan Wang⁴, Yu-Gang Zhou⁴, Qiang Li⁴, Yue Yang¹, Fang Tan¹, Xiao-Hui Zhang¹, Jie Zhang¹, Wen-Bo Mo^{1,2}, Jing-Qin Su¹, Wei-Min Zhou¹, Yu-Qiu Gu¹, Ming Zeng^{1,3,2,†} and Zong-Qing Zhao^{1,‡}

¹Science and Technology on Plasma Physics Laboratory,
Laser Fusion Research Center, CAEP, Mianyang 621900, China

²Department of Engineering Physics, Tsinghua University, Beijing 100084, China

³Key Laboratory of Particle and Radiation Imaging (Tsinghua University), Ministry of Education, Beijing 100084, China

⁴School of Information Engineering, Southwest University of Science and Technology, Mianyang 621010, China

Currently, with the advent of high-repetition-rate laser-plasma experiments, the demand for online diagnosis for the X-ray spectrum is increasing because the laser-plasma-generated X-ray spectrum is very important for characterizing electron dynamics and applications. In this study, scintillators and silicon PIN (P-type-Intrinsic-N-type semiconductor) diodes were used to construct a wideband online filter stack spectrometer. The X-ray sensor and filter arrangement was optimized using a genetic algorithm to minimize the condition number of the response matrix. Consequently, the unfolding error was significantly reduced based on numerical experiments. The detector responses were quantitatively calibrated by irradiating the scintillator and PIN diode with various nuclides and comparing the measured γ -ray peaks. A prototype 15-channel spectrometer was developed by integrating an X-ray detector with front- and back-end electronics. The prototype spectrometer could record X-ray pulse signals at a repetition rate of 1 kHz. Furthermore, an optimized spectrometer was employed to record the real-time spectra of laser-driven bremsstrahlung sources. This optimized spectrometer offers a compact solution for spectrum diagnostics of ultrashort X-ray pulses, exhibiting improved accuracy in terms of spectrum measurements and repetition rates, and could be widely used in next-generation high-repetition-rate high-power laser facilities.

Keywords: Filter stack spectrometer; Laser plasma diagnostics; X-ray diagnostics; Scintillator; PIN diode

I. INTRODUCTION

Laser-driven plasma-based electron accelerators and X-ray sources powered by ultra-intense laser technology have been extensively researched in recent years. With an accelerating gradient of approximately 100 GeV/m in laser plasma accelerators, electrons can be accelerated to hundreds of MeV within a few millimeters [1]. Subsequently, these electrons can generate X-rays through betatron radiation [2], inverse Compton scattering [3–5], and bremsstrahlung [6], thus providing tabletop alternatives to large-scale conventional accelerator-based X-ray sources. These X-ray sources have advantages such as femtosecond duration, micron-sized source dimensions, and a wide spectral range [7], thereby exhibiting tremendous potential for multiple applications [8], including biological radiography [9], non-destructive testing [10, 11], and high-energy-density physics [12, 13].

The research and application of laser-driven tabletop X-ray sources require a unique set of diagnostics [14]. Among them, X-ray spectrometers are particularly important as they characterize electron dynamics in plasma [4, 5, 15, 16] and are useful in various applications [13]. Multiple types of spectrometers have been developed to cover a wide range of pho-

ton energies, from a few keV to tens of MeV, in laser-plasma experiments. For X-rays below 30 keV, charge-coupled devices (CCDs) operating under single-photon counting mode provide high-resolution X-ray spectra by identifying individual X-ray photon signals in a single image frame [17, 18]. Crystal spectrometers can be employed for X-rays below 100 keV, and the spectrum can be measured by detecting the angular distribution of X-rays diffracted by the crystal [19, 20]. For X-rays with energies in the range of hundreds of keV, an electron-track-based spectrometer has been proposed that reconstructs X-ray energies by detecting Compton electron tracks and energies using silicon trackers [21]. For X-rays greater than 1 MeV, the Compton spectrometer converts the X-rays into electrons via forward Compton scattering. Compton electron spectra are measured using a magnetic spectrometer, from which X-ray spectra can be derived [22–26]. Although the aforementioned spectrometers are sensitive to X-rays within relatively narrow energy ranges, the filter stack spectrometer (FSS) enables the diagnosis of X-ray spectra over a wide band, typically ranging from tens of keV to hundreds of MeV. A FSS employs a stack of filters interlaced with X-ray sensors [27–29], and the characteristic parameters of the X-ray spectra can be reconstructed from the response matrix (RM) and sensor signals. Additionally, FSSs have the advantages of simple manufacturing and simple operation; therefore, they have been widely used in laser-plasma experiments.

Currently, many FSSs utilize image plates (IPs) as X-ray sensors [27–29] because of their reusability, high sensitivity to X-rays, versatility, and resistance to electromagnetic pulses [30, 31]. However, the IP signals must be read offline using an

* This work was partially supported by the Natural Science Foundation of China (Nos. 12004353, 11975214, 11991071, 11905202, 12175212, and 12120101005) and the Key Laboratory Foundation of the Science and Technology on Plasma Physics Laboratory (Nos. 6142A04200103 and 6142A0421010).

† Corresponding author, zengming@mail.tsinghua.edu.cn

‡ Corresponding author, zhaozongqing99@caep.ac.cn

IP scanner, which takes approximately 10 min for data reading. This offline readout time does not meet the requirements of high-repetition-rate laser-plasma experiments. Given the importance of high repetition rates in studying experimental laws and optimizing accelerators and X-ray sources [32–34], there is a need for online diagnosis of the wideband spectrum of laser-induced X-rays.

Scintillators and semiconductors are commonly used in X-ray sensors [35]. Scintillators convert X-rays into visible scintillation light, which can be easily transformed into electric signals using a photoelectric converter. In contrast, semiconductors convert X-rays into charge carriers (electrons and holes). Electric signals are generated at the electrode as the charge carriers drift under a bias voltage. The decay time of scintillators and the charge carrier drift time of semiconductors typically range from a few to hundreds of nanoseconds. Therefore, electrical signals can be recorded and processed online using an electric readout system. Consequently, an FSS constructed with scintillators or semiconductors would allow for a fast repetition rate, aligned with the current state-of-the-art and next-generation laser systems. Recently, online FSSs based on scintillators have been developed [36–39] utilizing CCDs or complementary metal-oxide-semiconductor (CMOS) cameras as photoelectric converters. Notably, scintillator-based FSSs have already been employed in experiments [40–42], demonstrating exceptional performance in wideband X/γ-ray detection. However, certain aspects of the currently developed online FSS techniques require further improvement.

First, the light collection efficiency is low because the lens of CCDs or CMOS cameras covers only a small solid angle. This limitation can result in high statistical uncertainties, particularly under conditions of low X-ray fluence. Second, the calibration and stability of the scintillation-light-collection efficiency pose challenges owing to the non-solid nature of light couplings. Finally, the FSS configuration has not been adequately optimized, resulting in a severely ill-conditioned RM. These limitations may contribute to a relatively large error in X-ray spectrum determination.

In this paper, we propose an optimized online fast X-ray spectroscopy system (FSS) and present its implementation herein. To address the ill-conditioned RM, we employed a genetic algorithm [43] to optimize the sensor and filter arrangement. To achieve robust light coupling and a high light collection efficiency, we utilized PIN diodes with large sensitive areas and low noise as the photoelectric converters. Furthermore, PIN diodes were employed as sensors in the channels closest to the X-ray sources, enabling the direct detection of low-energy X-rays and improving the unfolding accuracy within an energy range of tens to one hundred keV. The proposed configuration allows for direct calibration of the light-collection efficiency and alleviates the ill-conditioned nature of the RM. According to numerical experiments, the relative deviation of the true and unfolded spectra can be decreased to approximately 16%. The electrical signals from the PIN diodes are amplified using in-house built trans-impedance amplifiers (TIAs) and main amplifiers, and then digitized by a multi-channel data acquisition (DAQ) system based on the

DRS4 chip [44]. The proposed online FSS integrates filters, X-ray sensors, front-end electronics (FEE), and the DAQ system, resulting in a compact and user-friendly system. Notably, the proposed online FSS exhibits sensitivity to X-rays ranging from tens of keV to hundreds of MeV, enabling the recording of X-ray pulse signals at a repetition rate of 1 kHz. By contrast, CCD- or CMOS-based FSSs typically have a maximum repetition rate of 100 Hz [36]. Furthermore, the proposed online FSS demonstrates an energy measurement error of less than 1%, whereas traditional IP systems have a 20% energy measurement error [29], thereby providing a more accurate unfolding spectrum.

II. METHODOLOGY

A. Spectrometer optimization

The most significant drawback of the FSS is the ill-posed linear system, which results in substantial errors in spectrum measurements. Because the scintillator can function as both filter and sensor, parameters such as the layer thickness, number of layers, filter density, and scintillator density need to be finely tuned to alleviate the ill-conditioned nature of the RM. Rusby et al. [36] optimized their online FSS based on the difference in the scintillator output within the energy range of interest. The optimal scintillator should exhibit the largest difference in scintillator output. However, this optimization criterion was spectrum-dependent and the scintillator thicknesses were kept constant, limiting the optimization efficiency.

To propose a universal optimization method, we first establish a formal model for encoding an X-ray spectrum $S(E)$ into the experimental channel D_i for an N-channel FSS. The mathematical definitions and notation employed in this study are consistent with those used by Fehl et al. [45, 46]. D_i can be written as follows:

$$D_i = \int_0^{E_{\text{MAX}}} R_i(E)S(E)dE + \epsilon_i = d_i + \epsilon_i (i = 1, \dots, N), \quad (1)$$

where D_i represents the experimental channel data, $R_i(E)$ denotes the response function, d_i represents the noise-free channel data, and ϵ_i represents uncertainties and noise. Equation (1) can be expressed in vector-matrix notation as follows:

$$\mathbf{D} = \mathbf{R}\mathbf{S} + \Delta\mathbf{D} = \mathbf{d} + \Delta\mathbf{D}. \quad (2)$$

The errors that affect the unfolding accuracy can be divided into two parts. The first part is the perturbation $\Delta\mathbf{D}$ superimposed on \mathbf{D} during the data-gathering process, which includes factors such as statistical uncertainty, signal noise, digitization errors, and uncorrected signal baselines, among others. The second part is the bias between the experimentally measured or simulated RM and the actual RM, expressed as $\mathbb{R} \rightarrow \mathbb{R} + \Delta\mathbb{R}$. The presence of $\Delta\mathbb{R}$ can be attributed to drifts and uncertainties in the fitting parameters, such as the calibration of the light yield and light collection efficiency

discussed in Sect. II C. Because $(\Delta\mathbb{R})\mathbf{S}$ is analogous to $\Delta\mathbf{D}$ [46], only $\Delta\mathbf{D}$ is discussed here.

Solving Eq. (2) poses challenges because it is an ill-posed problem. Various unfolding algorithms can be employed to address this problem, including regularization methods, least-squares spectrum adjustment, parameter estimation, iterative unfolding methods, and the maximum entropy principle [47]. However, these unfolding algorithms often struggle to provide mathematically rigorous or realistic estimates of the error propagation relationship between the spectral unfolding error $\Delta\mathbf{S}$ and the data perturbation $\Delta\mathbf{D}$. Nevertheless, it is worth noting that the error propagation relationship between $\Delta\mathbf{S}$ and $\Delta\mathbf{D}$ is primarily determined via the response function \mathbb{R} . For instance, an upper-bound measure for $\Delta\mathbf{S}$ can be estimated from $\Delta\mathbf{D}$ and the condition number of the RM is denoted by $\text{cond}(\mathbb{R})$, as described in [45].

$$\|\Delta\mathbf{S}\|/\|\mathbf{S}\| \leq \text{cond}(\mathbb{R})\|\Delta\mathbf{D}\|/\|\mathbf{D}\|, \quad (3)$$

where $\|\mathbf{D}\| = (\sum_{i=1}^N D_i^2)^{\frac{1}{2}}$ represents the norm of \mathbf{D} . RM \mathbb{R} can be either a square or non-square matrix [59], and the condition number $\text{cond}(\mathbb{R})$ can be calculated via singular value decomposition. By reducing $\text{cond}(\mathbb{R})$, for example, by alleviating the ill-conditioned nature of the RM, the upper-bound measure of $\Delta\mathbf{S}$ can be lowered, resulting in improved precision in terms of the spectrum measurements. Furthermore, $\text{cond}(\mathbb{R})$ is determined solely by the FSS configuration. Hence, $\text{cond}(\mathbb{R})$ can serve as a measure of merit for FSS optimization, independent of the spectrum.

Another challenge in spectrometer optimization is the multi-parameter optimization problem. FSS typically comprises numerous filter and sensor layers, and the thickness and density (determined by the material) of each layer can affect $\text{cond}(\mathbb{R})$. Consequently, multiple parameters must be optimized. Owing to the practical limitations on the layer thickness for both the filter and sensor, as well as the absence of derivatives and linearity in this problem, the genetic algorithm is a suitable method for optimization.

Several factors restrict the range of the optimization parameters. In an FSS, filters and sensors closer to the X-ray source are typically thinner, whereas those farther away are thicker. This design ensures that most low-energy X-rays deposit their energy in the layers near the sources and high-energy X-rays do so in the layers farther away. Consequently, RM \mathbb{R} has a smaller condition number ($\text{cond}(\mathbb{R})$). To address the low light-collection efficiency of thin scintillators, which can result in significant statistical errors, sensors with a 300 μm depletion layer thickness, such as PIN diodes, were used in the layers near the X-ray source. For custom production convenience, the scintillators are made of $\text{Gd}_3\text{Al}_2\text{Ga}_3\text{O}_{12}$ (GAGG) [48], while the filters are made of aluminum or copper. After determining the number of layers, $\text{cond}(\mathbb{R})$ should be minimized because it is scale-dependent. Considering that the number of layers is a tradeoff between the applicable energy range and the complexity of the signal readout system, 15 layers were selected, including six PIN diodes and nine scintillators. The overall configuration of the proposed online FSS is listed in Table 1. The layer number represents the distance from the X-ray source with the filter closer to the source

in each layer. As an aluminum film of 50 μm is always used as the first layer for electromagnetic shielding, the parameters to be optimized are the filter thickness in layers 2–15 and the scintillator thickness in layers 7–15.

Table 1. General configuration of the proposed online FSS

Layer	Filter	Sensor	Layer	Filter	Sensor
1	Al	Si-PIN	9	Cu	GAGG
2	Al	Si-PIN	10	Cu	GAGG
3	Al	Si-PIN	11	Cu	GAGG
4	Al	Si-PIN	12	Cu	GAGG
5	Al	Si-PIN	13	Cu	GAGG
6	Al	Si-PIN	14	Cu	GAGG
7	Cu	GAGG	15	Cu	GAGG
8	Cu	GAGG			

A key aspect for implementing the genetic algorithm is the fitness assignment method. As the population consists of 2000 individuals and there are 300 iterations, approximately 6×10^5 $\text{cond}(\mathbb{R})$ calculations, i.e., RM calculations, are required. Accurately RM calculations using the Monte Carlo method [28, 36, 37] consume significant computational power. To reduce the computational power requirement, a simplified RM calculation model that utilizes the X-ray mass energy absorption coefficients and mass attenuation coefficient is proposed. First, the expected energy deposition of a single X-ray with energy E in the i -th sensor, denoted by $E_{\text{dep},i}(E)$, can be calculated as

$$E_{\text{dep},i}(E) = (1 - e^{-\mu_{\text{en},i}(E)s_i}) \cdot \prod_{j=1}^{i-1} e^{-\mu_j(E)s_j} \cdot \prod_{j=1}^i e^{-\mu_j(E)f_j} E, \quad (4)$$

where $\mu_{\text{en},i}(E)$ represents the X-ray mass energy absorption coefficient of the i -th sensor, $\mu_j(E)$ represents the X-ray mass attenuation coefficient of the j -th sensor or filter, s_j and f_j denote the thickness of the j -th sensor and filter, respectively. Thus, the RM equation can be written as

$$R_i(E) = E_{\text{dep},i}(E) \cdot \text{ESC}_i. \quad (5)$$

where ESC_i are the energy-signal coefficients of the i -th channel. For the PIN diode,

$$\text{ESC}_i = 1/3.62 \times q \times \rho_i, \quad (6)$$

where 3.62 eV is the pair creation energy of silicon [49], q is the elementary charge, and ρ is the gain of the electronics in ohm. For GAGG,

$$\text{ESC}_i = (\text{LY} \times \text{LCE} \times \text{QE})_i \times q \times \rho_i, \quad (7)$$

where LY is the light yield of GAGG, LCE is the light collection efficiency, and QE is the quantum efficiency of the photon detector. If we disregard the nonlinearity of the scintillator light yield and electronics, ESC_i becomes independent of the X-ray energy E . Therefore, the practical response equation to be solved can be derived using Eqs. (1) and (5) as follows:

$$\mathbf{D}/\text{ESC} = \mathbb{E}_{\text{dep}}\mathbf{S}_{\text{unfold}}. \quad (8)$$

where $\mathbf{S}_{\text{unfold}}$ is the spectral unfolding and \mathbb{E}_{dep} is the matrix notation of $E_{\text{dep},i}(E)$. An error $\Delta \mathbf{S}$ exists between $\mathbf{S}_{\text{unfold}}$ and the real X-ray spectrum \mathbf{S} owing to perturbation $\Delta \mathbf{D}$ in \mathbf{D} . In Eq. (8), \mathbb{E}_{dep} is equivalent to RM \mathbb{R} , and can be determined from Eq. (4). Therefore, the optimization process for reducing $\text{cond}(\mathbb{E}_{\text{dep}})$ is illustrated in Fig. 1.

The genetic algorithm was implemented using the Sheffield Genetic Algorithm toolbox [50]. The population consisted of 2000 individuals, with each individual containing 14 filter thicknesses and nine scintillator thicknesses. These thicknesses are represented as floating-point numbers and encoded as bit strings to create chromosomes. Each individual contained 24 binary chromosomes, representing the 14 filter thicknesses and nine scintillator thicknesses. To consider practical layer thickness limitations, lower and upper limits were set for the filters and scintillators, 0.01 and 50 mm and 2 and 50 mm, respectively. Each binary chromosome uses 20 bits to ensure sufficient precision. For the iterations, all filter thicknesses were set to zero, and any thickness below 0.1 mm was also set to zero. The generation gap, mutation probability, and crossover probability were set to 0.9, 0.01, and 0.7, respectively. The termination criterion was reached when the iteration time was 300.

The minimum and average $\text{Cond}(\mathbb{E}_{\text{dep}})$ values during the iterations are shown in Fig. 2. The optimal $\text{Cond}(\mathbb{E}_{\text{dep}})$ is approximately 4×10^4 , which represents a significant reduction compared with the unoptimized online FSS configuration. For instance, the previously reported CsI FSS [37] exhibited a $\text{Cond}(\mathbb{E}_{\text{dep}})$ of 2×10^{12} (considering 15 channels). The optimal configuration obtained during the iterations is listed in Table 2. The 0.01-mm precision is maintained, considering that the machining tolerance of the GAGG crystal is 0.02 mm.

Table 2. Optimized configuration of the proposed online FSS

Layer	Filter	Thickness (mm)	Sensor	Thickness (mm)
1	Al	0.05	Si-PIN	0.3
2	Al	0	Si-PIN	0.3
3	Al	0	Si-PIN	0.3
4	Al	2.82	Si-PIN	0.3
5	Al	9.95	Si-PIN	0.3
6	Al	24.34	Si-PIN	0.3
7	Cu	3.53	GAGG	2
8	Cu	10.07	GAGG	2
9	Cu	4.73	GAGG	4.44
10	Cu	6.97	GAGG	13.04
11	Cu	0.57	GAGG	12.15
12	Cu	13	GAGG	33.74
13	Cu	1.14	GAGG	21.65
14	Cu	18.24	GAGG	33.2
15	Cu	34.52	GAGG	50

It is worth noting that the optimization process using a simple RM calculation model has certain limitations. First, because the mass attenuation and mass X-ray absorption coefficients are available only within an energy range of 1 keV to 20 MeV, the optimization process considers X-rays ranging from 10 keV to 10 MeV. Second, it is well known that the simple

RM calculation model does not consider secondary effects, such as Compton scattering and pair production processes, which become dominant in photon-matter interactions starting at hundreds of keV. Consequently, the simple RM calculation model results deviate from the actual values above hundreds of keV. However, it still provides a reasonable estimation of the actual RM, and we demonstrated that optimization is an effective approach for achieving a partially optimized structure. This is evident from the significant reduction in the unfolding error, as demonstrated next.

B. Unfolding spectrometer response

Numerical experiments were conducted to test the unfolding procedure and evaluate the accuracy of the unfolded radiation spectra. Using Eqs. (2) and (5), the expected energy deposition \mathbb{E}_{dep} , X-ray spectrum \mathbf{S} , energy-signal coefficients \mathbf{ESC} , and perturbation $\Delta \mathbf{D}$ were calculated and modeled to simulate the channel data.

First, the optimized online FSS was modeled using GEANT4 [51], a simulation platform using the Monte Carlo method, to obtain an accurate \mathbb{E}_{dep} . The simulation model consists of the filters, sensors, scintillation photon detector, PIN diode carrier board, collimator, shielding, and other mechanical parts. The incident X-rays were simulated as pencil-like beams uniformly and randomly distributed within a 6-mm-diameter circle, matching the collimator diameter. The energy range of the incident X-rays was set from 10 keV to 200 MeV. For each energy bin, the X-ray energies were uniformly and randomly sampled and 10^7 X-rays were simulated. The energy deposition curves of the X-ray beams impinging on the online FSS, i.e., \mathbb{E}_{dep} , are shown in Fig. 3.

The X-ray spectrum \mathbf{S} is modeled as follows:

$$S(E) = S_{\text{Beta}}(E) + S_{\text{Brems}}(E) + S_{\text{BG}}(E), \quad (9)$$

where $S_{\text{Beta}}(E) = AE^\alpha \exp(-\beta E)$ represents the on-axis betatron component, $S_{\text{Brems}} = \frac{B}{E}(\nu - \ln(E))$ represents the on-axis bremsstrahlung component, and $S_{\text{BG}}(E) = C \exp(-\eta E)$ represents the background component [28, 52]. Note that E is in MeV. Parameters A , α , β , B , ν , C , and η define the shape of the curves and the fluence ratios of the three components. Specifically, they are set to 12.47, 0.768, 7.52, 4.09×10^{-4} , 3.88, 0.01, and 1, respectively. In this scenario, the betatron radiation critical and peak energies are 0.25 and 0.1 MeV, respectively, and the fluence ratio of the background component is 7%. This represents a typical betatron radiation spectrum with background [28]. Assuming X-ray energies ranging from 10 keV to 10 MeV and a total photon count of 10^5 , the simulated energy depositions in the online FSS channels were obtained by multiplying the expected energy deposition \mathbb{E}_{dep} by the photon count in each energy bin, $S(E)dE$.

\mathbf{ESC} can be estimated using Eqs. (6) and (7). GAGG-HL-type GAGG crystals manufactured by EPIC CRYSTAL Co., Ltd., with a light yield LY of 54000 photons/MeV were used in this study. The light-collection efficiency LCE was approximately 60% under typical packaging and optical cou-

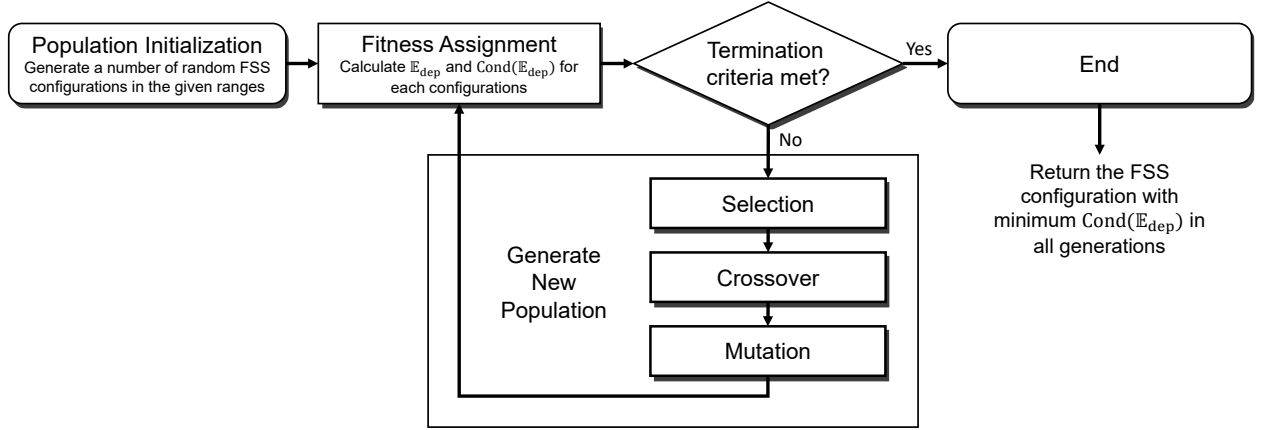


Fig. 1. Optimization process of the proposed online FSS using the genetic algorithm

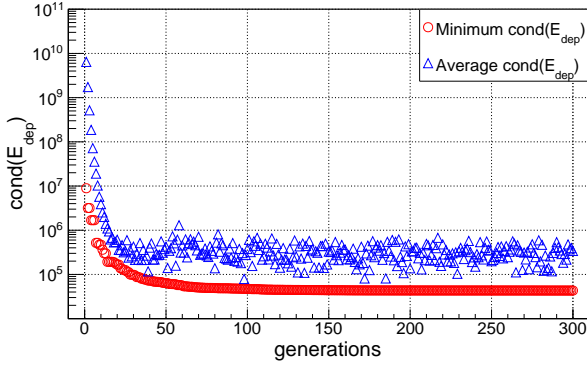


Fig. 2. (Color online) Evolution of $Cond(\mathbb{E}_{dep})$ during the genetic algorithm iterations

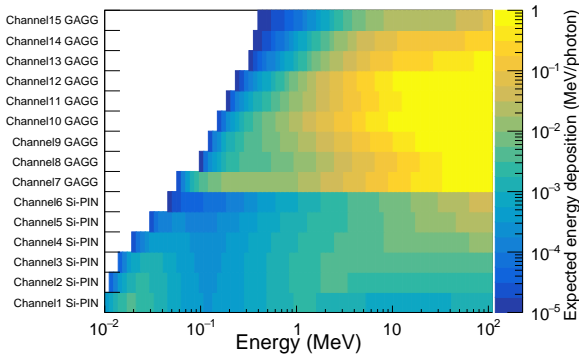


Fig. 3. (Color online) Response matrix expressed as \mathbb{E}_{dep} obtained via Monte Carlo simulations

efficiency QE of PIN diodes, such as the 0.3-mm Si-PIN, is approximately 90% at a wavelength of 530 nm. Because ESC may vary owing to the different scintillators, packaging, and optical couplings, it was experimentally calibrated as described in Sect. II C. The FEE gains (ρ) are the product of the gains of the TIAs and main amplifiers, which collectively determine the overall gain of the electronic unit. The gains of the TIAs and main amplifiers were determined individually to ensure that the signal amplitudes conformed to the dynamic ranges of each stage. A detailed discussion of ρ is provided in Sect. III B and the values are listed in Table 4.

The perturbation ΔD is primarily caused by the statistical uncertainty $\sigma(E)_{st}$, where E represents the energy deposition in the detector, and the electronic noise σ_{noise} . The total perturbation σ_{total} is calculated as $\sigma_{total} = \sqrt{\sigma(E)_{st}^2 + \sigma_{noise}^2}$. The statistical uncertainty in the PIN diode channels can be estimated using $\sigma(E)_{st} = 2.355\sqrt{F \cdot E \cdot W}$, where $F = 0.12$ is the Fano factor and $W = 3.62$ eV is the energy required for the formation of a charge carrier pair. Statistical uncertainties in the GAGG channels were estimated based on a previous calibration experiment conducted in our laboratory using radioactive sources [53]. In particular, $\sigma(E)_{st} = 0.09 \cdot 662 \times 10^3 \cdot \sqrt{\frac{662 \times 10^3}{E}}$. The electronic noise model is complex and beyond the scope of this study. The calculation method for the electronic noise in a high-speed waveform-sampling detector is described in detail in [54]. According to Cang et al. [54], when the pulse amplitude fully utilizes the ADC range and the integration time window is 150 ns, the electronic noise reaches approximately 0.12%. Considering that our time integration window is 600 ns and the pulse amplitude may vary from pulse to pulse, a 1% electronic noise error estimation is reasonable. Therefore, an electronic noise of $\sigma_{noise} = 0.01 \times D_i$ is applied to all channels, where D_i represents the noise-free channel data.

Based on the simulated channel data, D_{sim} , the unfolded X-ray spectrum was obtained by solving Eq. (8) using the expectation-maximization method [55]. The convergence degree is indicated by the normalized mean absolute distance (MAD) between the fitting and simulated channel data.

$$MAD_{\text{data}} = \frac{1}{N} \sum \frac{|D_{i,\text{fit}} - D_{i,\text{sim}}|}{D_{i,\text{sim}}}, \quad (10)$$

where N denotes the number of channels. Using a constant function of unity as the initial guess for $S_{\text{unfold}}(E)dE$, the fitting errors for different numbers of iterations are plotted in Fig. 4(a). In the case of the optimized GAGG array (represented by the red open circles), the fitting error initially decreases rapidly to a low level within the first few steps and eventually reaches $< 1\%$ after 50 steps. The deviation between the unfolded spectrum and the spectrum model function is also indicated by the normalized MAD between them.

$$MAD_{\text{spec}} = \frac{1}{M} \sum \frac{|S_{\text{unfold}}(E)dE - S(E)dE|}{S(E)dE}, \quad (11)$$

where M denotes the number of energy bins. As shown in Fig. 4(b), the divergence can reach a minimum of approximately 16% in an energy range of 10 keV to 10 MeV when the fitting converges. In this study, 100 iteration steps were chosen, which is sufficiently large to observe the convergence properties, obtain a reasonable spectrum shape, and fit the response of the FSS, as shown in Fig. 5. It should be noted that the choice of the unfolding algorithm can significantly affect the unfolding results, and the expectation-maximization method was selected because of its ability to avoid the need for many additional constraints and its greater universality.

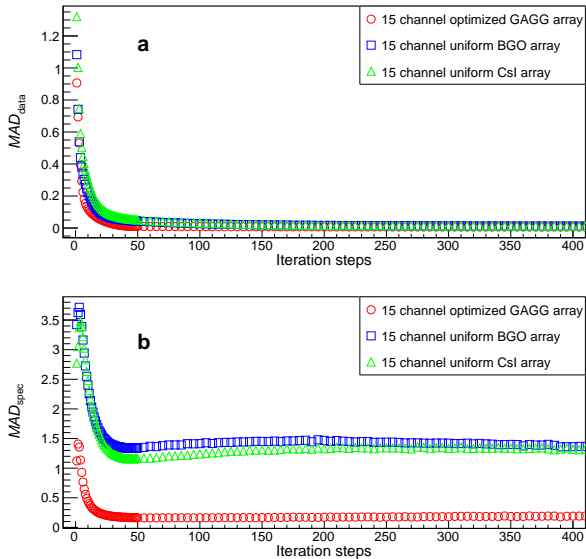


Fig. 4. (Color online) (a) Converge curve and (b) unfolding error for three kinds of online FSSs

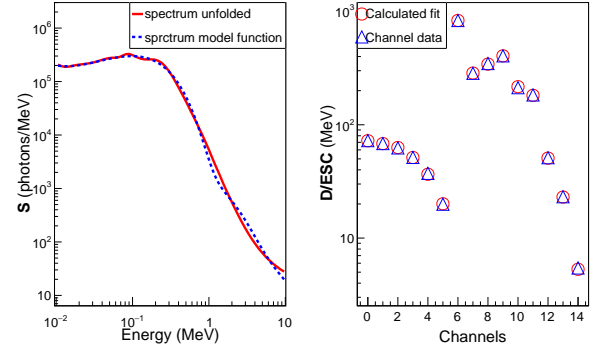


Fig. 5. (Color online) Fitting data (right) plotted with the corresponding spectra (left)

al. [36] were also simulated following the aforementioned procedure. The channel number and noise level were kept the same as those in the GAGG array, that is, 15 channels. The thickness of the BGO crystals was 0.2 cm. The condition numbers for the CsI and BGO arrays were 2×10^{12} and 1×10^{12} , respectively. The corresponding minimum fitting errors were 115% for the CsI array and 133% for the BGO array, respectively, as shown in Fig. 4. The unfolding error of the optimized GAGG array was significantly reduced compared to that of the CsI and BGO arrays with uniform thickness.

C. Quantitative calibration of the spectrometer response

An accurate RM determination is of vital importance for precise spectrum unfolding. In Eq. (5), $E_{\text{dep},i}(E)$ can be precisely obtained through Monte Carlo simulations [28, 36, 37]. However, ESC must be experimentally calibrated for scintillator channels because the light yield LY and light collection efficiency LCE can vary depending on the scintillators, packages, and optical couplings, making it challenging to model and calculate them.

The most challenging aspect of the experimental calibration campaign for LY and LCE is determining the energy deposition in the scintillators. Behm et al. [37] performed an experimental calibration by measuring the scintillation signal resulting from bremsstrahlung interactions. They theoretically calculated the bremsstrahlung X-ray beam in GEANT4 by simulating the collision of a typical electron beam with a 9-mm-thick piece of lead. The energy deposition in the CsI array was then determined using GEANT4. Rusby et al. [36] calibrated their online FSS by exposing the detector to radiation sources for an extended period of time and integrating the camera images. Energy deposition during this period was also determined via GEANT4 simulation.

In the optimized online FSS, a PIN diode with a 0.3-mm Si-PIN was also used as the scintillation photon detector. The 300- μm depletion layer of the 0.3-mm Si-PIN allows us to obtain $LY \times LCE \times QE$ by comparing the full-energy peaks of the radioactive sources. One source directly irradiates the PIN

diode 0.3-mm Si-PIN, while the other irradiates the GAGG scintillator [56]. The energy deposition in the scintillators, that is, the gamma ray lines of the radioactive sources, can be accurately determined, thereby providing more reliable calibration results.

The calibration experiment utilized ^{241}Am with a 59.5-keV line and ^{22}Na with a 1274.5-keV line. Charge-sensitive preamplifiers were used instead of TIAs to amplify the signals induced by the radioactive sources. An example of the spectrum measured during the experiment for a single channel is shown in Fig. 6. The peak positions were obtained by fitting the experimental spectrum using a Gaussian curve superimposed on a second-order polynomial background, denoted by the green lines; the background is represented by the brown lines.

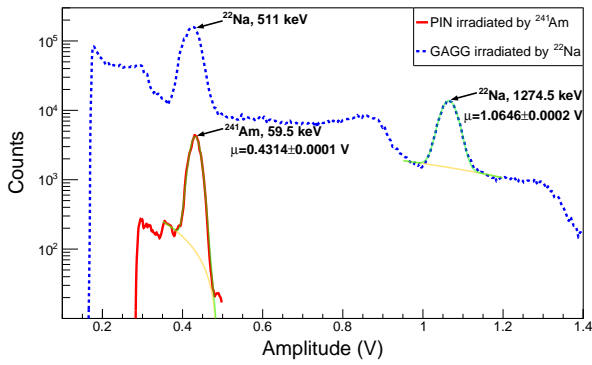


Fig. 6. (Color online) Spectra obtained during the calibration experiment for one channel

As the readout electronics are identical for GAGG and PIN diodes, according to Eqs. (5)–(7), $LY \times LCE \times QE$ can be calculated as follows:

$$LY \times LCE \times QE = \frac{P_{\text{GAGG}} E_{\text{dep,PIN}}}{3.62[\text{eV}] \cdot P_{\text{PIN}} E_{\text{dep,GAGG}}}, \quad (12)$$

where P_{GAGG} and P_{PIN} are the fitting peak positions in the experimental spectrum, $E_{\text{dep,GAGG}}$ and $E_{\text{dep,PIN}}$ are the energy depositions in GAGG and PIN diodes, which are 1274.5 and 59.5 keV, respectively. The corresponding spectra are shown in Fig. 6, P_{GAGG} and P_{PIN} are 1.0646 ± 0.0002 and 0.4314 ± 0.0001 V, respectively; therefore, $LY \times LCE \times QE = 31826 \pm 5$ electrons/MeV.

III. IMPLEMENTATION

An online FSS prototype was built and calibrated using the aforementioned methods. A schematic of the online FSS prototype is shown in Fig. 7. Similar to classic radiation detectors [57], the FSS prototype comprises sensors, FEE, a DAQ system, and various software. The prototype comprises six PIN diode channels and nine GAGG scintillator channels as X-ray sensors, which are interleaved with aluminum and copper filters. The collimator and laser sight are located in front of the PIN diode sensors, and the laser sight is replaced with

an outer collimator once the FSS is mounted. The scintillators are coupled with PIN diodes as photon detectors. The signal output pins of the PIN diodes are connected to an FEE board. The following DAQ board provides the capability for 16-channel waveform digitization and communication. In addition, a power board supplies low-noise ± 5 V and 70 V power to the FEE and PIN diodes. To avoid interference from scattered X-rays, the filters and X-ray sensors are shielded by a 1-cm-thick lead layer and a 1-cm-diameter aperture allowing for X-ray incidence. The aperture is covered with a 50- μm -thick aluminum foil for electromagnetic shielding. The electronics are housed in an enclosed copper and aluminum box for electromagnetic shielding. The external interface includes only a 12-V power supply cable and a USB communication cable.

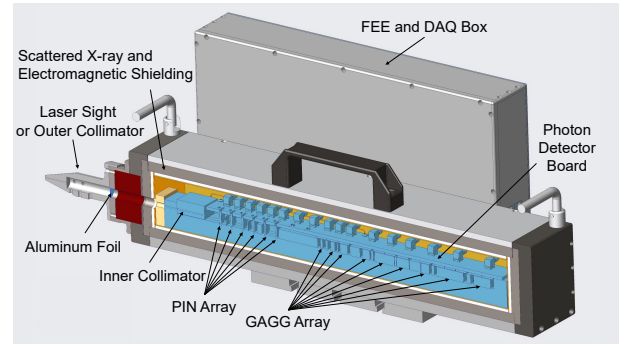


Fig. 7. (Color online) Cross-sectional view of the online FSS prototype

A. Filter and sensor unit

GAGG scintillators were chosen because of their good mechanical characteristics, non-hygroscopic properties, high light yield (30–70 ph/keV), and fast decay times (~ 100 ns). The scintillators had front faces measuring $1\text{ cm} \times 1\text{ cm}$ with variable thicknesses. The filter and scintillator configurations are listed in Table 3. The prototype configuration was obtained using the original version of our optimization code without proper constraints on the thickness, resulting in a configuration different from that listed in Table 2. Nevertheless, the condition number of the prototype response matrix is 6×10^5 , which is close to the optimized condition number presented in Sect. II A (compared with the uniform-thickness configuration), and an improved performance is expected.

The reflection layers of the scintillators are enhanced specular reflectors (ESRs), 65- μm polymers with high reflectance ($>98\%$) manufactured by 3M. The ESRs were cut into specific shapes to allow the coupling of the scintillation light from the side of the scintillators. The scintillators were fixed to an aluminum frame and interleaved with filters, as shown in Fig. 8.

The scintillation light output is bright when the scintillators are irradiated by laser-induced brilliant X-ray pulses, for example, $>5 \times 10^7$ scintillation photons ($10^3\text{ MeV} \times 54000$

Table 3. Configuration of the online FSS prototype

Layer	Filter	Thickness (mm)	Sensor	Thickness (mm)
1	Al	0.05	Si-PIN	0.3
2	Al	0.59	Si-PIN	0.3
3	Al	0	Si-PIN	0.3
4	Cu	0.11	Si-PIN	0.3
5	Al	0	Si-PIN	0.3
6	Al	5.5	Si-PIN	0.3
7	Cu	45.55	GAGG	2.6
8	Cu	2.63	GAGG	4.85
9	Cu	1.3	GAGG	8.67
10	Cu	11.59	GAGG	8.58
11	Cu	2.52	GAGG	23.26
12	Cu	2.06	GAGG	14.26
13	Cu	12.94	GAGG	9.49
14	Cu	3.16	GAGG	31.23
15	Cu	4.91	GAGG	19.58

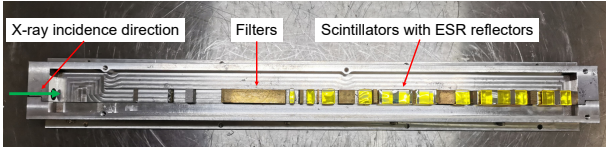


Fig. 8. (Color online) Filters and scintillators used in the prototype

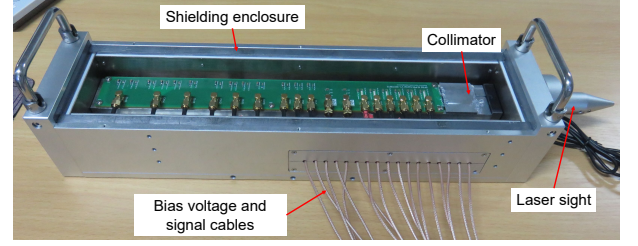
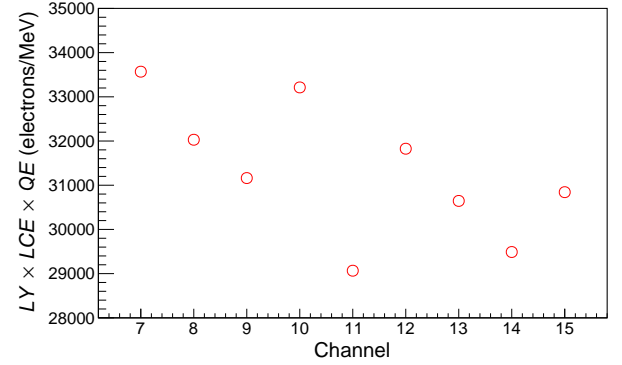


Fig. 10. (Color online) Filter and sensor unit

Fig. 11. Experimentally calibrated $LY \times LCE \times QE$ for the nine GAGG scintillation channels of the prototype

528 photons/MeV) per channel per pulse. A non-multiplying photon detector is suitable for collecting scintillation light. To improve the light-collection efficiency and coupling stability, a PIN diode with a large sensitive area ($1 \text{ cm} \times 1 \text{ cm}$) was used as the photon detector, and the PIN diodes were directly coupled with the scintillators using optical grease. As there are six PIN diode channels used as X-ray sensors, all PIN diodes are mounted on one PIN diode carrier board vertically or horizontally, as shown in Fig. 9.

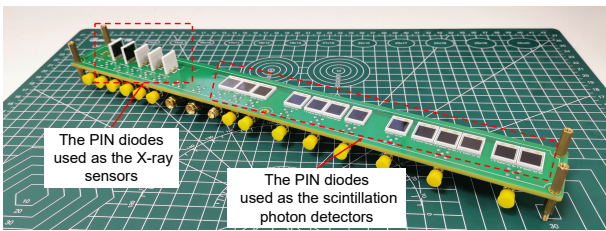


Fig. 9. (Color online) PIN diodes and their carrier board

537 The sensors, filters, and PIN diodes were placed in an X-ray- and electromagnetic-shielding enclosure along with the collimator and laser sight, making up the filter and sensor unit, as shown in Fig. 10. Bias voltages and electric signals were applied or elicited using coaxial cables.

542 Using the calibration method described in Section II C, the $LY \times LCE \times QE$ values for the nine GAGG scintillation channels were calibrated experimentally, as shown in Fig. 11. Error bars are not visible in this figure because of the low peak fitting error.

B. Electronics unit

548 The PIN diode signal is fed to a TIA via alternating current (AC) coupling, and a standard high-speed amplifier with a 1.6-GHz gain bandwidth product is adopted as the TIA amplifier. A 2000-ohm resistor connects the cathode of the PIN diode to the ground, serving as the direct-current (DC) path, which can limit the current of the PIN diode and increase the system reliability. The TIA is followed by the main amplifier, which adjusts the voltage amplitude to match the dynamic range of the DAQ system. In addition to the 16-channel TIAs and main amplifiers, the FEE board includes a trigger circuit to generate an inner trigger signal for the DAQ system.

559 The FEE circuit gains are determined to ensure that the signal amplitude is within the dynamic range of each circuit stage. First, the energy deposition per pulse in the PIN diodes and scintillators was calculated using GEANT4. The spectrum of the X-ray source was modeled using Eq. (9) with a photon fluence of 1×10^{11} photons/sr/pulse, and is located 1 m away from the collimator of the online FSS. Therefore, the number of X-ray photons passing through the collimating aperture is 2.8×10^6 per pulse.

568 The temporal waveforms were calculated using the transient response model, which includes the GAGG scintillation light, PIN diode output current, and output voltage of each circuit stage. The PIN diode was treated as a second-order Butterworth low-pass filter (LPF) with a 40-MHz -3 dB bandwidth [58]. The transient response of the GAGG scintillator can be expressed as a single exponential decay signal with a decay time of 100 ns, and the TIA can also be treated as

a second-order Butterworth LPF with a -3 dB bandwidth of $\sqrt{GBP/(2\pi R_F C_D)}$ [53], where GBP is the 1.6-GHz gain bandwidth product, R_F is the feedback resistance, and C_D is the input capacitance of the TIA. C_D is mainly attributed to the terminal capacitance of the PIN diodes and the stray capacitance of the cables, and is in the order of ~ 100 pF. The main amplifier was designed as an inverting second-order voltage-controlled voltage source LPF with a 10-MHz -3 dB bandwidth. The simulated FEE output waveform obtained by the transient response model is plotted along with the experimental waveform measured in the laser-plasma experiment, as shown in Fig. 12. The simulated waveform is in good agreement with the experimental waveform, e.g., the relative difference in the peak amplitudes is less than 2% when the integrals from 130 to 700 ns are equal (with the same energy depositions), thus validating the transient response model built in this study.

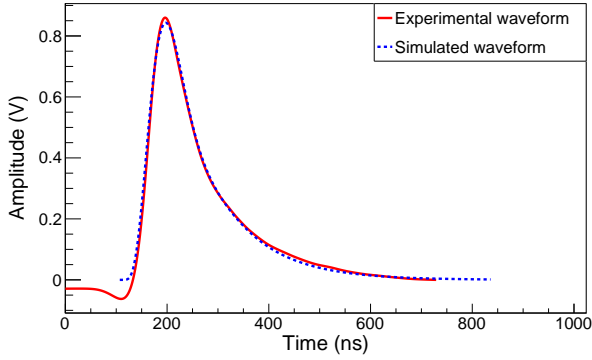


Fig. 12. (Color online) Simulated and experimental waveforms of the FEE output

As the voltage output swing of the TIA is 0–3 V and the input dynamic range of the DAQ system is 1 V, the main amplifier gains are determined to fully utilize the dynamic range of the DAQ system, which is 0.32. Then, using the transient response model, the TIA gains are determined to ensure that the peak amplitudes of the 15-channel TIA outputs are in the order of 500 mV. The results are presented in Table 4, with the TIA and main amplifier gains listed on the left and right sides of the multiplication signs, respectively. The main purpose of this section is to describe the hardware design. As the X-ray fluence can vary significantly in different laser-plasma experiments, the FEE is designed as a plug-in module so that the gains can be determined using the described methods and can be easily changed.

Table 4. FEE gains

Channels	1–6	7–12	13–15
ρ in ohm	100×0.32	200×0.32	1000×0.32

To preserve the temporal waveform information and enable flexible digital signal processing, a commercial 16-channel high-speed analog-to-digital conversion module based on DRS4 chips was adopted as the DAQ system. The DAQ system provides a 1-GHz sample rate, a 1024-sample acquisition

window (equivalent to $1.024 \mu\text{s}$ at 1 GHz), and a 30-MB/s transfer rate (using the USB 2.0 protocol). Given that the GAGG decay time is 100 ns, a $1.024\text{-}\mu\text{s}$ acquisition window is sufficient to capture the complete waveform. The online FSS system requires a high repetition rate of several hundred kHz. However, the DAQ data transfer rate imposes a limitation of approximately 1 kHz, calculated as 30 MB/s divided by "16 channels \times 12 bits/sample \times 1024 samples/channel/pulse," resulting in 1220 pulses/s. In future campaigns in which higher repetition rates may be available, upgrading the data transfer protocol would allow for a faster online FSS system.

IV. BREMSSTRAHLUNG EXPERIMENT

To test the functionality of the online FSS design, the prototype was implemented in a laser-driven bremsstrahlung experiment to facilitate the diagnosis of the X/ γ -ray spectrum. Laser-driven bremsstrahlung offers several advantages, including high energy, micro-spot size, and a compact system scale, thereby leading to a significant improvement in the resolution of high-energy computed tomography (CT) [61]. These bremsstrahlung sources typically operate at high repetition rates. Real-time monitoring of the spectrum plays a vital role in evaluating the stability of the radiation source and aids in CT image reconstruction.

The experiment was conducted utilizing a high-repetition laser system with a 100-TW power, as shown in Fig. 13. During the experiment, a laser pulse was focused onto the gas chamber to generate high-energy low-emittance electron beams via a laser wakefield acceleration (LWFA) mechanism. The laser beam was focused onto a $25\text{-}\mu\text{m}$ spot using an off-axis parabolic mirror with a 2-m focal length, which captured approximately 58% of the laser energy. By reducing the pulse duration to as short as 24 fs, a peak intensity of approximately $4.4 \times 10^{18} \text{ W/cm}^2$ was achieved at the target point with an energy input of 2 J. A 4-mm-long gas chamber served as the target for generating the electron beams. Pure nitrogen was used to enhance the plasma density and increase the total charge via ionized injection. The molecular density reached approximately $1.4 \times 10^{19} \text{ cm}^{-3}$ at a pressure of 1000 kPa.

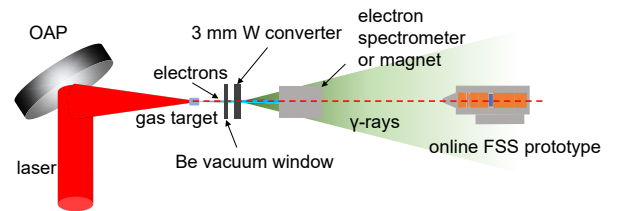


Fig. 13. (Color online) Bremsstrahlung experimental setup

First, the LWFA electron beam properties were assessed using an electron spectrometer. The electron beam traversed a $300\text{-}\mu\text{m}$ -thick beryllium vacuum window, with the electron spectrometer positioned downstream of the vacuum window. The measured electron spectra are shown in Fig. 14.

656 The LWFA electron beam exhibited a divergence of approx-
 657 imately 7 mrad and charge of approximately 1000 pC. The
 658 energy of the electron beam ranged from 5 to 150 MeV.

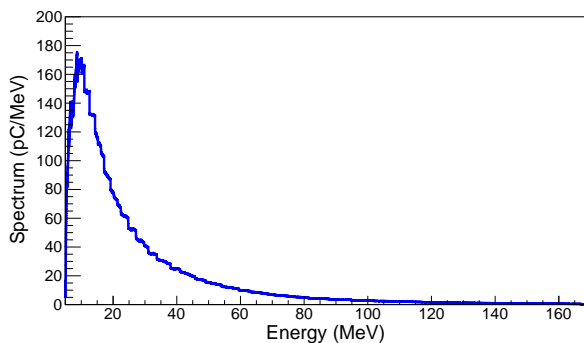


Fig. 14. Spectrum of the LWFA electron beam

659 Subsequently, the electron spectrometer was dismantled,
 660 and a 3-mm tungsten converter was positioned 25 cm from
 661 the gas target to generate intense bremsstrahlung radiation.
 662 To deflect the transmission electrons, a 10-cm magnet with
 663 a magnetic field strength of 0.8 Tesla was placed behind the
 664 converter. The online FSS, situated at a distance of 1.2 m
 665 from the tungsten converter, was responsible for detecting the
 666 on-axis bremsstrahlung spectrum. The waveform measure-
 667 ments from a single shot are presented in Fig. 15. For
 668 the GAGG channels, the waveforms were integrated over a
 669 time window of 100–700 ns, while for the PIN diode chan-
 670 nels, integration was performed for 100–250 ns. These in-
 671 tegrated waveforms constituted the experimental channel data
 672 and are denoted by **D**. There are also some pulse-shaping
 673 methods that can be used to calculate **D** if the X-ray sources
 674 have a very high repetition rate and the waveforms accumu-
 675 late [62, 63]. The expected energy deposition (\mathbb{E}_{dep}) was
 676 obtained via Geant4 simulation and the energy-signal coef-
 677 ficients (ESC) were derived and computed using Eqs. (6)
 678 and (7). The spectra were obtained by solving Eq. (8) via the
 679 expectation-maximization method with 100 iteration steps.

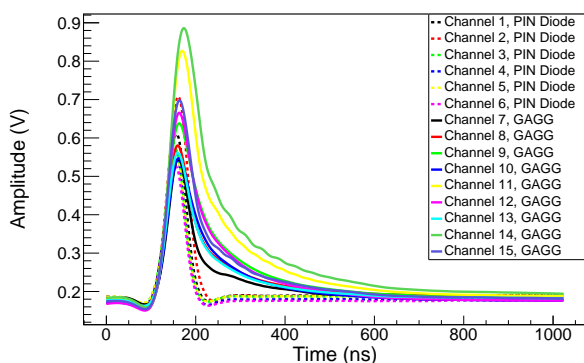


Fig. 15. (Color online) Measured waveforms

680 The bremsstrahlung was generated at a repetition rate of
 681 0.1 Hz, and the real-time responses of the online FSS were
 682 recorded. From the collected waveforms, a subset of five

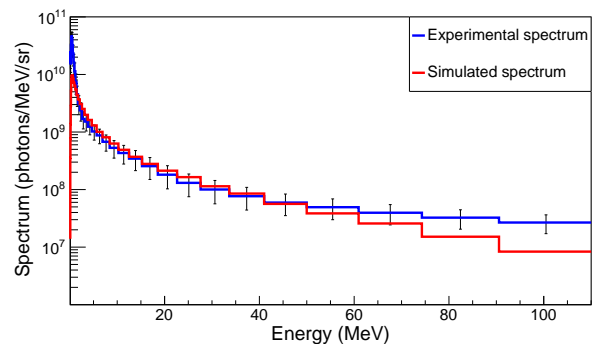


Fig. 16. (Color online) Spectra unfolded in the preliminary experiment

683 shots exhibiting suitable pulse amplitudes was selected for
 684 subsequent unfolding to obtain the bremsstrahlung spectra.
 685 The average bremsstrahlung spectrum and its standard devi-
 686 ation for the five shots are depicted by the blue line in Fig.
 687 16. In addition, the bremsstrahlung spectrum was simulated
 688 using GEANT4. In the simulation, 5×10^9 electrons were in-
 689 jected into a 3-mm tungsten converter with the electron spec-
 690 tral shape shown in Fig. 14. The on-axis bremsstrahlung
 691 within the acceptance angle of the online FSS (approximately
 692 10^{-5} rad) was recorded. The simulated bremsstrahlung spec-
 693 trum is depicted by the red line in Fig. 16. The experimental
 694 spectrum exhibits good agreement with the simulated spec-
 695 trum, particularly in the energy range of 1–80 MeV. The in-
 696 cident electrons in the simulation possess a total charge of
 697 800 pC, which is consistent with the charge measured us-
 698 ing the electron spectrometer. It is worth noting that the
 699 bremsstrahlung spectrum from a thick converter is challeng-
 700 ing to model using analytical formulas owing to the signif-
 701 icant bremsstrahlung absorption by the converter itself [64].
 702 Consequently, the parameter-fitting unfolding techniques em-
 703 ployed in previous studies [28, 29, 40] are not applicable to
 704 this particular bremsstrahlung. However, by enhancing the
 705 FSS structure design and improving the data acquisition ac-
 706 curacy, the expectation-maximization method can be employed
 707 to unfold the spectrum with higher precision. The recon-
 708 structed photon flux reduction caused by self-absorption be-
 709 low 1 MeV matched well and was consistent with the simu-
 710 lated spectrum. Nevertheless, a notable discrepancy exists
 711 between the simulation and experimental results at approx-
 712 imately 1 MeV. This discrepancy may be attributed to the
 713 presence of scattered background in the experiment, which
 714 was not considered in the Geant4 simulation.

V. CONCLUSION

716 In this paper, we propose an optimization method that uti-
 717 lizes a genetic algorithm to address the ill-posed nature of the
 718 FSS system. The condition number of the response matrix
 719 (RM) is employed as the optimization criterion. To enhance
 720 the unfolding accuracy across energy bands ranging from tens
 721 of keV to tens of MeV, we employed high-density GAGG

scintillators and silicon PIN diodes. Monte Carlo simulation results demonstrated that the optimized FSS configuration yielded significantly improved accuracy when measuring typical spectra within this energy range.

The optimized online FSS featuring PIN diodes as scintillation photon detectors was successfully implemented. This choice enhances the light-collection efficiency and ensures stable coupling, further improving the unfolding accuracy. In addition, the use of PIN diodes facilitates the quantitative calibration of light yields and light collection efficiencies. The electrical signals from the PIN diodes were amplified and digitized using a custom front-end electronics (FEE) module and a commercial data acquisition (DAQ) card. The current online FSS prototype operates at a repetition rate of 1 kHz with the potential for further enhancement by increasing the data transfer rate of the DAQ card, e.g., using an 80-MB/s optical link interface or a USB 3.0 interface. By eliminating the need for an image plate (IP) scanner or a high-speed CCD/C-MOS, the proposed online FSS system offers the advantages of cost-effectiveness and compactness.

The functionality of the online FSS prototype was validated through a laser-driven bremsstrahlung experiment. The

bremsstrahlung spectrum was recorded in real time and exhibited good agreement with the simulated bremsstrahlung spectrum. In future work, we will conduct additional system test experiments and enhance the electromagnetic compatibility to develop a low-noise system with high unfolding accuracy. Additionally, we will investigate methodologies for identifying improved FSS structures by leveraging supercomputers for Monte Carlo RM calculations and optimizing parameters such as the number of layers. These investigations will be conducted with the aim of satisfying the accuracy requirements associated with diverse experimental scenarios. As the demand for high repetition rates and accuracy increases, this optimized, integrated, compact, and cost-effective online FSS technique is promising for advancing laser-plasma research and application.

VI. ACKNOWLEDGEMENT

The authors thank Zhi-Meng Zhang and Bo Zhang for their assistance in the experiments.

-
- [1] E. Esarey, C. B. Schroeder, and W. P. Leemans, "Physics of laser-driven plasma-based electron accelerators," *Rev. Mod. Phys.*, 81, 1229(2009). DOI: 10.1103/RevModPhys.81.1229
 - [2] E. Esarey, B. A. Shadwick, P. Catravas et al., "Synchrotron radiation from electron beams in plasma-focusing channels," *Phys. Rev. E*, 65, 056505(2002). DOI: 10.1103/PhysRevE.65.056505
 - [3] K. Ta Phuoc, S. Corde, C. Thauray et al., "All-optical Compton gamma-ray source," *Nat. Photonics*, 6, 308(2012). DOI: 10.1038/nphoton.2012.82
 - [4] G. Sarri, D. Corvan, W. Schumaker et al., "Ultrahigh Brilliance Multi-MeV gamma-Ray Beams from Nonlinear Relativistic Thomson Scattering," *Phys. Rev. Lett.*, 113, 224801(2014). DOI: 10.1103/PhysRevLett.113.224801
 - [5] W. Yan, C. Fruhling, G. Golovin et al., "High-order multiphoton Thomson scattering," *Nat. Photonics*, 11, 514(2017). DOI: 10.1038/nphoton.2017.100
 - [6] S. Cipiccia, S. M. Wiggins, R. P. Shanks et al., "A tuneable ultra-compact high-power, ultra-short pulsed, bright gamma-ray source based on bremsstrahlung radiation from laser-plasma accelerated electrons," *J. Appl. Phys.*, 111, 063302(2012). DOI: 10.1063/1.3693537
 - [7] S. Corde, K. Ta Phuoc, G. Lambert et al., "Femtosecond x rays from laser-plasma accelerators," *Rev. Mod. Phys.*, 85, 1(2013). DOI: 10.1103/RevModPhys.85.1
 - [8] F. Albert and A. G. R. Thomas, "Applications of laser wakefield accelerator-based light sources," *Plasma Phys. Controlled Fusion*, 58, 103001(2016). DOI: 10.1088/0741-3335/58/10/103001
 - [9] B. Guo, X. Zhang, J. Zhang et al., "High-resolution phase-contrast imaging of biological specimens using a stable betatron X-ray source in the multiple-exposure mode," *Sci. Rep.*, 9, 7796(2019). DOI: 10.1038/s41598-019-42834-2
 - [10] C. P. Jones, C. M. Brenner, C. A. Stitt et al., "Evaluating laser-driven Bremsstrahlung radiation sources for imaging and analysis of nuclear waste packages," *J. Hazard. Mater.*, 318, 694(2016). DOI: 10.1016/j.jhazmat.2016.07.057
 - [11] Y. Yang, Y.-C. Wu, L. Li et al., "Design and characterization of high energy micro-CT with a laser-based X-ray source," *Results Phys.*, 14, 102382(2019). DOI: 10.1016/j.rinp.2019.102382
 - [12] R. Tommasini, C. Bailey, D. K. Bradley et al., "Short pulse, high resolution, backlighters for point projection high-energy radiography at the National Ignition Facility," *Phys. Plasmas*, 24, 053104(2017). DOI: 10.1063/1.4983137
 - [13] C. Tian, M. Yu, L. Shan et al., "Radiography of direct drive double shell targets with hard x-rays generated by a short pulse laser," *Nucl. Fusion*, 59, 046012(2019). DOI: 10.1088/1741-4326/aafe30
 - [14] M. Downer, R. Zgadzaj, A. Debus et al., "Diagnostics for plasma-based electron accelerators," *Rev. Mod. Phys.*, 90, 035002(2018). DOI: 10.1103/RevModPhys.90.035002
 - [15] S. Kneip, S. R. Nagel, C. Bellei et al., "Observation of Synchrotron Radiation from Electrons Accelerated in a Petawatt-Laser-Generated Plasma Cavity," *Phys. Rev. Lett.*, 100, 105006(2008). DOI: 10.1103/PhysRevLett.100.105006
 - [16] S. Kneip, C. McGuffey, J. L. Martins et al., "Bright spatially coherent synchrotron X-rays from a table-top source," *Nat. Phys.*, 6, 980(2010). DOI: 10.1038/nphys1789
 - [17] Y. H. Yan, L. Wei, X. L. Wen et al., "Calibration and Monte Carlo simulation of a single-photon counting charge-coupled device for single-shot X-ray spectrum measurements," *Chin. Opt. Lett.*, 11, 4(2013). DOI: 10.3788/col201311.110401
 - [18] C. Stoeckl, W. Theobald, T. C. Sangster et al., "Operation of a single-photon-counting x-ray charge-coupled device camera spectrometer in a petawatt environment," *Rev. Sci. Instrum.*, 75, 3705(2004). DOI: 10.1063/1.1788867
 - [19] M.-h. Yu, G.-y. Hu, N. An et al., "Hard x-ray transmission curved crystal spectrometers (10-100 keV) for laser fusion experiments at the ShenGuang-III laser facility," *High Power*

- Laser Sci. Eng.*, 4, e2(2016). DOI: 10.1017/hpl.2015.36
- [20] Z. Chi, L. Yan, Z. Zhang et al., “Diffraction based method to reconstruct the spectrum of the Thomson scattering x-ray source,” *Rev. Sci. Instrum.*, 88, 045110(2017). DOI: 10.1063/1.4981131
- [21] J. Wen, M. Yu, Y. Wu et al., “Diagnostics for ultra-short X-ray pulses using silicon trackers,” *Nucl. Instrum. Methods Phys. Res., Sect. A*, 1014, 165754(2021). DOI: 10.1016/j.nima.2021.165754
- [22] S. Singh, R. Versaci, A. L. Garcia et al., “Compact high energy x-ray spectrometer based on forward Compton scattering for high intensity laser plasma experiments,” *Rev. Sci. Instrum.*, 89, 7(2018). DOI: 10.1063/1.5040979
- [23] S. Cipiccia, S. M. Wiggins, D. Maneuski et al., “Compton scattering for spectroscopic detection of ultra-fast, high flux, broad energy range X-rays,” *Rev. Sci. Instrum.*, 84, 113302(2013). DOI: 10.1063/1.4825374
- [24] A. E. Gehring, M. A. Espy, T. J. Haines et al., “Determining x-ray spectra of radiographic sources with a Compton spectrometer,” *Radiation Detectors: Systems and Applications Xv*, Proc. SPIE 9215, 921508(2014). DOI: 10.1117/12.2065588
- [25] D. J. Corvan, G. Sarri, and M. Zepf, “Design of a compact spectrometer for high-flux MeV gamma-ray beams,” *Rev. Sci. Instrum.*, 85, 065119(2014). DOI: 10.1063/1.4884643
- [26] D. Haden, G. Golovin, W. Yan et al., “High energy X-ray Compton spectroscopy via iterative reconstruction,” *Nucl. Instrum. Methods Phys. Res., Sect. A*, 951, 163032(2020). DOI: 10.1016/j.nima.2019.163032
- [27] C. Courtois, R. Edwards, A. C. La Fontaine et al., “Characterization of a MeV Bremsstrahlung x-ray source produced from a high intensity laser for high areal density object radiography,” *Phys. Plasmas*, 20, 9(2013). DOI: 10.1063/1.4818505
- [28] J. H. Jeon, K. Nakajima, H. T. Kim et al., “A broadband gamma-ray spectrometry using novel unfolding algorithms for characterization of laser wakefield-generated betatron radiation,” *Rev. Sci. Instrum.*, 86, 9(2015). DOI: 10.1063/1.4939014
- [29] A. Hannasch, A. Laso Garcia, M. LaBerge et al., “Compact spectroscopy of keV to MeV X-rays from a laser wakefield accelerator,” *Sci. Rep.*, 11, 14368(2021). DOI: 10.1038/s41598-021-93689-5
- [30] A. L. Meadowcroft, C. D. Bentley, and E. N. Stott, “Evaluation of the sensitivity and fading characteristics of an image plate system for x-ray diagnostics,” *Rev. Sci. Instrum.*, 79, 113102(2008). DOI: 10.1063/1.3013123
- [31] T. Bonnet, M. Comet, D. Denis-Petit et al., “Response functions of imaging plates to photons, electrons and 4He particles,” *Rev. Sci. Instrum.*, 84, 103510(2013). DOI: 10.1063/1.4826084
- [32] P. W. Hatfield, J. A. Gaffney, G. J. Anderson et al., “The data-driven future of high-energy-density physics,” *Nature*, 593, 351(2021). DOI: 10.1038/s41586-021-03382-w
- [33] T. Ma, D. Mariscal, R. Anirudh et al., “Accelerating the rate of discovery: toward high-repetition-rate HED science,” *Plasma Phys. Controlled Fusion*, 63, 104003(2021). DOI: 10.1088/1361-6587/ac1f67
- [34] Qi LIU, Haitao WANG, Haisheng CHEN et al. “Development of the electron gun filament power supply for small size betatron (in Chinese)” *NUCL. TECH.*, 45, 110401(2022). DOI: 10.11889/j.0253-3219.2022.hjs.45.110401.
- [35] C. Grupen and B. Shwartz, *Particle Detectors*.
- [36] D. R. Rusby, C. D. Armstrong, C. M. Brenner et al., “Novel scintillator-based x-ray spectrometer for use on high repetition laser plasma interaction experiments,” *Rev. Sci. Instrum.*, 89, 8(2018). DOI: 10.1063/1.5019213
- [37] K. T. Behm, J. M. Cole, A. S. Joglekar et al., “A spectrometer for ultrashort gamma-ray pulses with photon energies greater than 10 MeV,” *Rev. Sci. Instrum.*, 89, 9(2018). DOI: 10.1063/1.5056248
- [38] V. Stránský, V. Istokskaia, R. Versaci et al., “Development, optimization, and calibration of an active electromagnetic calorimeter for pulsed radiation spectrometry,” *J. Instrum.*, 16, 08060(2021). DOI: 10.1088/1748-0221/16/08/P08060
- [39] V. Istokskaia, V. Stránský, L. Giuffrida et al., “Experimental tests and signal unfolding of a scintillator calorimeter for laser-plasma characterization,” *J. Instrum.*, 16, 02006(2021). DOI: 10.1088/1748-0221/16/02/T02006
- [40] J. M. Cole, K. T. Behm, E. Gerstmayr et al., “Experimental Evidence of Radiation Reaction in the Collision of a High-Intensity Laser Pulse with a Laser-Wakefield Accelerated Electron Beam,” *Phys. Rev. X*, 8, 011020(2018). DOI: 10.1103/PhysRevX.8.011020
- [41] K. Poder, M. Tamburini, G. Sarri et al., “Experimental Signatures of the Quantum Nature of Radiation Reaction in the Field of an Ultraintense Laser,” *Phys. Rev. X*, 8, 031004(2018). DOI: 10.1103/PhysRevX.8.031004
- [42] C. I. D. Underwood, C. D. Baird, C. D. Murphy et al., “Development of control mechanisms for a laser wakefield accelerator-driven bremsstrahlung x-ray source for advanced radiographic imaging,” *Plasma Phys. Controlled Fusion*, 62, 124002(2020). DOI: 10.1088/1361-6587/abbebe
- [43] D. Goldberg, “Genetic Algorithm in Search, Optimization, and Machine Learning,” *Addison-Wesley, Reading, Massachusetts*, 1989.
- [44] M. Bitossi, R. Paoletti, and D. Tescaro, “Ultra-Fast Sampling and Data Acquisition Using the DRS4 Waveform Digitizer,” *IEEE Trans. Nucl. Sci.*, 63, 2309(2016). DOI: 10.1109/TNS.2016.2578963
- [45] D. L. Fehl, G. A. Chandler, W. A. Stygar et al., “Characterization and error analysis of an N X N unfolding procedure applied to filtered, photoelectric x-ray detector arrays. I. Formulation and testing,” *Phys. Rev. Spec. Top.-Accel. Beams*, 13, 120402(2010). DOI: 10.1103/PhysRevSTAB.13.120402
- [46] D. L. Fehl, G. A. Chandler, W. A. Stygar et al., “Characterization and error analysis of an N X N unfolding procedure applied to filtered, photoelectric x-ray detector arrays. II. Error analysis and generalization,” *Phys. Rev. Spec. Top.-Accel. Beams*, 13, 120403(2010). DOI: 10.1103/PhysRevSTAB.13.120403
- [47] M. Reginatto, “Overview of spectral unfolding techniques and uncertainty estimation,” *Radiat. Meas.*, 45, 1323(2010). DOI: 10.1016/j.radmeas.2010.06.016
- [48] J. Iwanowska, L. Swiderski, T. Szczesniak et al., “Performance of cerium-doped Gd₃Al₂Ga₃O₁₂ (GAGG:Ce) scintillator in gamma-ray spectrometry,” *Nucl. Instrum. Methods Phys. Res., Sect. A*, 712, 34(2013). DOI: 10.1016/j.nima.2013.01.064
- [49] A. Owens and A. Peacock, “Compound semiconductor radiation detectors,” *Nucl. Instrum. Methods Phys. Res., Sect. A*, 531, 18(2004). DOI: 10.1016/j.nima.2004.05.071
- [50] A. Chipperfield, P. Fleming, and H. Pohlheim, “A genetic algorithm toolbox for MATLAB,” *Proceedings of the International Conference on Systems Engineering*, 200(1994).
- [51] S. Agostinelli, J. Allison, K. Amako et al., “Geant4—a simulation toolkit,” *Nucl. Instrum. Methods Phys. Res., Sect. A*, 506, 250(2003). DOI: 10.1016/S0168-9002(03)01368-8
- [52] W. Schumaker, G. Sarri, M. Vargas et al., “Measurements of high-energy radiation generation from laser-wakefield acceler-

- ated electron beams,” *Phys. Plasmas*, 21, 056704(2014). DOI: 10.1063/1.4875336
- [53] J.-X. Wen, X.-T. Zheng, J.-D. Yu et al., “Compact CubeSat Gamma-ray detector for GRID mission,” *Nucl. Sci. Tech.*, 32, 99(2021). DOI: 10.1007/s41365-021-00937-4
- [54] J. Cang, T. Xue, M. Zeng et al., “Optimal design of waveform digitisers for both energy resolution and pulse shape discrimination,” *Nucl. Instrum. Methods Phys. Res., Sect. A*, 888, 96(2018). DOI: 10.1016/j.nima.2018.01.064
- [55] L. Zhang, G. Zhang, Z. Chen et al., “X-ray spectrum estimation from transmission measurements using the expectation maximization method,” *IEEE Nucl. Sci. Symp. Conf. Rec.*, 4, 3089(2007). DOI: 10.1109/NSSMIC.2007.4436783
- [56] L. Meng, D. Ramsden, V. Chirkin et al., “The design and performance of a large-volume spherical CsI(Tl) scintillation counter for gamma-ray spectroscopy,” *Nucl. Instrum. Methods Phys. Res., Sect. A*, 485, 468(2002). DOI: 10.1016/S0168-9002(01)02107-6
- [57] Song YANG, Xiaoquan ZHANG, Changming DENG, et al. “Design of portable multi-function radiation detection system” *NUCL. TECH.*, 45, 110403(2022). DOI: 10.11889/j.0253-3219.2022.hjs.45.110403.
- [58] “0.3 mm Si-PIN datasheet.”
- [59] Golub, G. H. and Loan, Cf Van. *Matrix computations* (3rd ed.), 1996
- [60] C. Zulick, B. Hou, F. Dollar et al., “High resolution bremsstrahlung and fast electron characterization in ultra-fast intense laser–solid interactions,” *New J. Phys.*, 15, 123038(2013). DOI: 10.1088/1367-2630/15/12/123038
- [61] Y. C. Wu, B. Zhu, G. Li et al., “Towards high-energy, high-resolution computed tomography via a laser driven micro-spot gamma-ray source,” *Sci. Rep.*, 8, 15888(2018). DOI: 10.1038/s41598-018-33844-7
- [62] Xueyuan WANG, Jianbin ZHOU, Jianfeng HE et al. “Impulse response shaping method for nuclear pulses based on derivative operations” *NUCL. TECH.*, 45, 070403(2022). DOI: 10.11889/j.0253-3219.2022.hjs.45.070403.
- [63] Xiaoyan YANG, Xu HONG, Jianbin ZHOU et al. “Gaussian pulse shaping algorithm for dual exponential signals based on wavelet transform” *NUCL. TECH.*, 46, 050403(2023). DOI:10.11889/j.0253-3219.2023.hjs.46.050403.
- [64] C. Robert Emigh, “Thick Target Bremsstrahlung Theory,” *Technical report of Los Alamos Scientific Laboratory of the University of California.*